Eur. Phys. J. E (2015) **38**: 122
DOI 10.1140/epje/i2015-15122-4

THE EUROPEAN PHYSICAL JOURNAL E

Regular Article

Theoretical study of actin layers attachment and separation

Sophie Marbach[1,2,a], Amélie Luise Godeau[4,5], Daniel Riveline[4,5], Jean-François Joanny[1,3,b], and Jacques Prost[1]

[1] Physico-Chimie Curie (Institut Curie, Cnrs UMR 168, UPMC), Institut Curie Centre de Recherche, 26, rue de l'Ulm, 75005, Paris, France
[2] ICFP, Physics Department, Ecole Normale Supérieure de Paris, 24 rue Lhomond, 75005, Paris, France
[3] ESPCI, 10 rue Vauquelin, 75005, Paris, France
[4] Laboratory of Cell Physics, Institut de Science et d'Ingénierie Supramoléculaires, Institut de Génétique et de Biologie Moléculaire et Cellulaire, Université de Strasbourg and Centre National de la Recherche Scientifique UMR 7006, Strasbourg, France
[5] Development and Stem Cells Program, Institut de Génétique et de Biologie Moléculaire et Cellulaire, Centre National de la Recherche Scientifique UMR 7104, Institut National de la Santé et de la Recherche Médicale (U964), Université de Strasbourg, Illkirch, France

Received 23 February 2015 and Received in final form 18 June 2015
Published online: 25 November 2015 –

Abstract. We use the theory of active gels to study theoretically the merging and separation of two actin dense layers akin to cortical layers of animal cells. The layers bind at a distance equal to twice the thickness of a free layer, thus forming a single dense layer, similar in this sense to a *lamellipodium*. When that unique layer is stretched apart, it is resilient to break apart up to a critical length larger than twice the thickness of a free layer. We show that this behavior can result from the high contractile properties of the actomyosin gel due to the activity of myosin molecular motors. Furthermore, we establish that the stability of the stretched single layer is highly dependent on the properties of the gel. Indeed, the nematic order of the actin filaments along the polymerizing membranes is a destabilizing factor.

1 Introduction

Fundamental biological processes such as adhesion, migration, and division of living animal cells strongly depend on the mechanics and the activity of their cytoskeleton. The cytoskeleton has a complex structure made of several components. It is generally accepted that the mechanical properties of animal cells essentially depend on the actomyosin component of the cytoskeleton, which is responsible for stress generation, and controls the response of cells to external mechanical perturbations [1, 2]. The actomyosin cytoskeleton has received much experimental [3, 4] and theoretical attention [5, 6]. It is composed of a dense meshwork of semi-flexible actin filaments interacting with myosin motor mini-filaments and actin-associated proteins. It is located in many cells in the vicinity of the cell membrane [7] where it forms the so-called cortical layer [8, 9]. Myosin motors hydrolyze adenosine triphosphate (ATP) molecules and can produce work. They crosslink actin filaments and create active contractile stresses in the actomyosin gel [10].

A hydrodynamic description that captures the behavior of active gels on large length and time scales was established to describe in particular the dynamics of the actomyosin gel [11–13]. It has been successfully applied to various situations: the discovery of spontaneous flows [14,15], spontaneous waves [16] and more recently to the closure of the contractile ring during cytokinesis [6,17]. The interaction of two layers of actomyosin gel has to our knowledge never been theoretically investigated. It is however of critical interest as a first step to understand the formation of a *lamellipodium* during cell motility. The *lamellipodium* is a dense layer of actin protruding from the main cytoskeletal structure of the cell body. Although actin flow inside the *lamellipodium* has been studied [18], the understanding of the precise shape of the protrusion linked to its structure remains to be explored.

In this work we are interested in the effect of the active contraction of actin gels on the interaction between two actin cortical layers. A recent theoretical work [5] has shown that the key element for the formation of a condensed actin layer in a stationary state at the membrane surface is the contractility of the actomyosin gel induced by the myosin molecular motors. In the cortical layer, in a simplified description, actin is treadmilling: it polymerizes at the cell membrane and depolymerizes in the bulk of the layer. Within the theory of active gels, the layer thickness is determined by the ratio between the polymerization velocity and the depolymerization rate of actin [5]. It is clear

[a] e-mail: sophie@marbach.fr
[b] e-mail: jean-francois.joanny@curie.fr

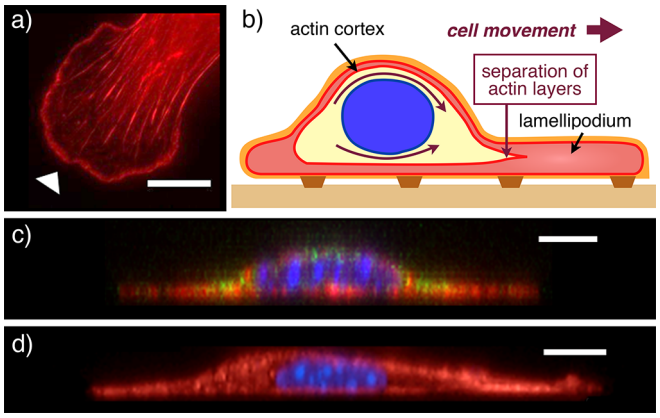

Fig. 1. a) *Lamellipodium* (at the arrowhead) promoted with incubation with 100 μM C8-BPA for 10 min (scale bar: 5 μm). b) Schematic of the cell contour. The cell moves in the direction of the *lamellipodium*. At the inner edge, the dense actin bundle is separated into two layers to form the actin cortex. c) Symmetric cell along the z-axis. C8-BPA was added 80 min after cell resuspension using trypsin treatment (scale bar: 5 μm). d) Non-symmetric cell along the z-axis. C8-BPA was added 10 min on spread cells (scale bar: 10 μm). F-actin is labeled in red in a), c), d), myosin in green in c), the nucleus in blue in c), d). See appendix A for details.

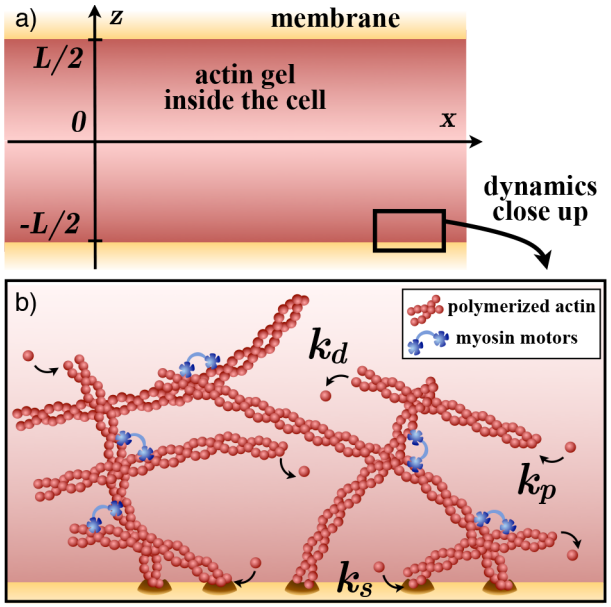

Fig. 2. a) Illustration of two interacting layers. The schematic shows two infinite planar membranes located at a distance L. The actin gel is distributed in between. The dynamics of polymerization and interaction close to the membrane are illustrated in b): Actin polymers are nucleated from the membrane surface at rate k_s. Polymerization and depolymerization of the polymers happen in the bulk at rate k_p and k_d, respectively. Myosin motors (blue stars) act as active cross-linkers between actin polymers, giving strong contractile properties to the gel.

that the interplay between contractility and average depolymerization impacts the interaction between two close layers.

Experimentally, dense actin can be observed in the *lamellipodium*. The lamellipodial protrusion is mainly generated by continuous growth of actin filaments from the leading edge [19] (see figs. 1(a) and (b)). Synthetic polyamines C8-BPA were recently shown to promote the growth of *lamellipodia* within minutes [20] (see fig. 1(a)). We used them and visualized the cell cortex along the z-axis on single spread cells with different experiments, as presented in figs. 1(c) and (d). These acquisitions demonstrate that the actomyosin cortex is spanning the cell contour and that there are multiple locations where the cytoplasm between layers presents a dense actin content. An important goal is therefore to understand how one single dense layer of actin (as in the *lamellipodium* at the cell front) can separate into two layers of actin cortex (see fig. 1(b)) and vice versa. To study the merging and separation of actin cortical layers we generalize here the hydrodynamic description of active gels to the case of two infinite planar membranes facing each other. We restrict the study to flat membrane surfaces. In the following we show that in the case of highly contractile actomyosin gels, with a high myosin activity and relatively low depolymerization rate, the merging and separation process is hysteretic. Contractility is the driving force, either maintaining separated layers firmly condensed near the membranes, or preventing a stretched single layer, similar to the *lamellipodium*, from breaking apart.

This paper is organized as follows. In sect. 2 we present the hydrodynamic equations for an actin gel between two infinite planar membranes, in a two-dimensional geometry. We then solve these equations in sect. 3 in the one-dimensional steady state. We study precisely the actin density between the layers as a function of the distance between the membranes, upon a change in the gel contractility. Finally we discuss in sect. 4 the stability of a single "stretched" layer in the presence of both isotropic and anisotropic contractility.

2 Hydrodynamic description

We present here the hydrodynamic equations governing the temporal and spatial dynamics of an assembling active actin gel. The gel and the solvent are localized between two planar membranes located at $z = -L/2$ and $z = L/2$, as shown in fig. 2(a). We assume locally planar membranes because the typical thickness of the actin gel in a cell (200–500 nm) is very small compared to the cell curvature radius (1 μm or more), except at the *lamellipodium* outer front. We restrict ourselves to a symmetric case, where the properties of the actin cortex are the same near each membrane. As suggested by the experiments, we assume furthermore that the gel is assembled by actin polymerization at the membrane surface at a rate k_s (see fig. 2(b), in the main body [21] and also in the *lamellipodium* [22]). The polymerization at the membrane is promoted by nucleating proteins [7]. Away from the surface, the actin gel assembles by elongation of existing filaments or by nucleation of new filaments and disassembles

because of monomer removal at the filament minus-ends or by filament severing. In our coarse-grained approximation, we model elongation and nucleation by a single effective polymerization rate k_p, which takes into account the bulk nucleating proteins, and disassembly by a single depolymerization rate k_d.

The whole system lies in the cytoplasm which acts as a reservoir containing, among other molecules, myosin free motors and actin monomers. Myosin molecular motors assemble as minifilaments and act as cross-links between actin filaments, thus generating mechanical stress in the filamentous network. Following the approach of [5] we limit ourselves to the case where the exchange of motors between the actin network and the solvent is so fast that we can assume chemical equilibrium. Motor diffusion is also assumed to be fast enough that the concentration of free motors in the solvent is constant. In a first approximation, the concentration of motors bound to actin is then proportional to the local density of actin monomers assembled into polymers.

The actin gel possesses a polarization field dependent on the local orientation of the filaments. The orientational order is in general nematic with the filaments oriented on average parallel to the surface but we consider also the isotropic case for the sake of generality.

We model the direction of each filament by a unit vector in Cartesian coordinates: $\boldsymbol{p}(x,y,z,t) = (\cos(\varphi)\sin(\theta)+\delta p_x)\boldsymbol{e_x}+(\sin(\varphi)\sin(\theta)+\delta p_y)\boldsymbol{e_y}+(\cos(\theta)+\delta p_z)\boldsymbol{e_z}$ with φ and θ the usual spherical coordinates and δp_x, δp_y and δp_z represent small fluctuations. φ is uniformly distributed (no preferred direction in the plane parallel to the membrane surface) in $[0, 2\pi]$, and θ may have a more complex distribution.

The nematic tensor is defined as $Q_{\alpha\beta} = \langle p_\alpha p_\beta - \frac{1}{3}p^2\delta_{\alpha\beta}\rangle$, where the average is a local average over the filament orientation. It reads at a $O(\delta p_{x,y,z})$:

$$Q = \begin{pmatrix} \frac{\langle\sin^2(\theta)\rangle}{2} - \frac{1}{3} & 0 & 0 \\ 0 & \frac{\langle\sin^2(\theta)\rangle}{2} - \frac{1}{3} & 0 \\ 0 & 0 & \langle\cos^2(\theta)\rangle - \frac{1}{3} \end{pmatrix}. \tag{1}$$

For further simplicity, we also consider that the gel is homogeneous in the y direction along the membrane, so that its properties only depend on the z and x coordinates.

2.1 Mass conservation

The density ρ of actin monomers assembled into polymers follows the conservation law:

$$\partial_t\rho + \partial_\alpha(\rho v_\alpha) = k_p - k_d\rho, \tag{2}$$

where $\boldsymbol{v}$ is the gel velocity field. We adopt Einstein's summation convention. The rates k_p and k_d can depend on the local actin density and on the local stresses in the gel. Such dependences were considered in the description of actin gels in [23, 24]. In our study, these dependences do not add physical content, and do not change the main results. The rates can also depend on the membrane considered, wether it is the free membrane or the one attached to the substrate, or wether it is the membrane in the main cell body or in the *lamellipodium*. Because we do not intend to describe the longitudinal profile of the *lamellipodium* in this paper, we restrict ourselves to the case where k_p and k_d are uniform constants in the following. We introduce in particular $\rho_\infty = k_p/k_d$, which measures the density ρ far from any boundaries and in a gel at steady state.

The fact that polymerization occurs also at the membrane surface with a surface rate k_s yields the boundary condition $\rho v_z|_{z=-L/2} = -\rho v_z|_{z=L/2} = v_p\rho_0$, where ρ_0 is the density of the actin gel at the surface and $v_p = k_s\delta$ is the polymerization velocity, δ being the effective size of an actin monomer. The density ρ_0 and the polymerization velocity v_p depend, among other factors, on the density of nucleating sites at the membrane. We consider that the boundary conditions are invariant by translation along x, so that ρ_0 and v_p are constant.

2.2 Force balance

We need yet another equation to characterize the mechanical equilibrium and the molecular fluxes in the system. We combine here multiple approaches on the theory of active permeating gels [5, 11–13, 25] to derive equations that are relevant in our case. In the following, we give only the general methodology to derive the equations. In our system the thermodynamic fluxes involved are the stress tensor σ, the time derivative of the elastic strain tensor in the gel, the relative current between the actin gel and the solvent $\boldsymbol{j} = \rho(\boldsymbol{v} - \boldsymbol{v_s})$, and the rate r of ATP consumption. The conjugated forces are the gradient of the relative chemical potential $\bar{\mu}$ between gel and solvent, the velocity gradient, the partial stress tensor of the gel and the activity of the system. Active processes in the system are essentially driven by the hydrolysis of ATP into adenosine diphosphate (ADP) and inorganic phosphate P_i, with chemical potentials μ_{ATP}, μ_{ADP} and μ_{P_i} respectively. We then measure the system's activity through $\Delta\mu = \mu_{\mathrm{ATP}} - \mu_{\mathrm{ADP}} - \mu_{P_i}$.

The general theory of active gels then uses the Onsager linear relation between fluxes and forces. Here, we give only the final equation for the relative current between actin gel and solvent for an apolar active gel

$$j_\alpha \equiv \rho(v_\alpha - v_{s,\alpha}) = -\gamma\partial_\alpha\overline{\mu} + \chi\partial_\beta\sigma_{\alpha\beta}, \tag{3}$$

with γ and χ two transport coefficients, and $\boldsymbol{v_s}$ the velocity field of the solvent.

In eq. (3), we consider that the Onsager coefficients are independent of the nematic order of the gel; the viscosity for instance is isotropic. The general theory includes other anisotropic terms that we ignore here. As the filaments can present anisotropic ordering, we must consider the

contribution of $Q_{\alpha\beta}$ to the stress tensor

$$2\eta v_{\alpha\beta} = \left(1 + \tau \frac{\mathrm{D}}{\mathrm{D}t}\right)\left(\sigma_{\alpha\beta} + \zeta' \Delta\mu Q_{\alpha\beta} + \zeta \Delta\mu \delta_{\alpha\beta}\right), \quad (4)$$

where $v_{\alpha\beta} = \frac{1}{2}(\partial_\alpha v_\beta + \partial_\beta v_\alpha)$, $\frac{\mathrm{D}}{\mathrm{D}t}$ is the convective time derivative, and τ is the viscoelastic relaxation time. The active coefficients ζ and ζ' denote the contributions of the active stress to the partial stress tensor. They are negative in the cell cortex because experimentally, activity leads to contractile stresses, and they depend on the gel density ρ. Equation (4) is a generalization of the Maxwell model for an active gel with nematic order. For the actin cortex, we consider that the experimental time scales are large compared to the viscoelastic relaxation time, so that we can neglect the convective time derivative.

We rewrite the term involving the relative chemical potential $\bar{\mu}$ in eq. (3), using the Gibbs-Duhem equation $\mathrm{d}\tilde{\Pi} = \rho \mathrm{d}\bar{\mu}$ that gives the evolution of the osmotic pressure $\tilde{\Pi}$ as a function of $\bar{\mu}$ in the case where the total volume of the system is constant (independent of composition, and incompressible). We then define an effective osmotic pressure, adding the active terms: $\Pi_{\alpha\beta} = \tilde{\Pi}\delta_{\alpha\beta} + \zeta \Delta\mu Q_{\alpha\beta} + \zeta \Delta\mu \delta_{\alpha\beta}$. With $\gamma = \chi\rho$, eq. (3) can be rewritten as

$$\frac{\rho}{\chi}(v_\alpha - v_{s,\alpha}) = 2\partial_\beta(\eta v_{\alpha\beta}) - \partial_\beta \Pi_{\alpha\beta}. \quad (5)$$

We proceed using the same approximation as in [5] to neglect the permeation current. The permeation constant ρ/χ can be estimated as η_s/ξ^2, where ξ is the gel mesh size and η_s the solvent viscosity. We then compare the two competing dissipative mechanisms, namely the gel viscosity and the permeation of the solvent through the actin gel. This comparison defines a permeation length $L_p = (\eta\chi\rho^{-1})^{1/2} = (\eta/\eta_s)^{1/2}\xi$. The experiments of [26] allow us to estimate $\eta_s \sim 10^3$ Pa s (effective viscosity measured for reference parameters of the actin gel). We take a solvent viscosity of 10^{-3} Pa s (close to water). With typical mesh sizes ξ of a few tens of nanometers, we obtain a permeation length of the order of tens of microns. This permeation length is sufficiently large compared to the thickness of the cortex. This argument allows us to neglect the left-hand side of eq. (5) compared to the viscous dissipation term if we consider the dynamics on length scales smaller than the permeation length scale.

From now on, we consider the gel density ρ and the gel velocity $\boldsymbol{v}$ as the only hydrodynamic variables. All quantities are considered to be invariant in the y direction, with no velocity along the y axis. Consequently, we write $\boldsymbol{v}$ as the vector $(u, 0, v)$. The projections of the constitutive eqs. (2) and (5) on the x and z axis read

$$\begin{cases} \partial_t \rho + \partial_z(\rho v) + \partial_x(\rho u) = -k_d(\rho - \rho_\infty), \\ \partial_z\left(\eta(\partial_x v + \partial_z u)\right) + 2\partial_x(\eta \partial_x u) - \partial_x \Pi_x = 0, \\ \partial_x\left(\eta(\partial_z u + \partial_x v)\right) + 2\,\partial_z(\eta \partial_z v) - \partial_z \Pi_z = 0, \end{cases} \quad (6)$$

with, using eq. (1)

$$\Pi_x = \tilde{\Pi} + \Delta\mu\zeta_x, \qquad \Pi_z = \tilde{\Pi} + \Delta\mu\zeta_z,$$
$$\zeta_x = \zeta + \zeta'\left(\frac{\langle \sin^2(\theta)\rangle}{2} - \frac{1}{3}\right),$$
$$\zeta_z = \zeta + \zeta'\left(\langle \cos^2(\theta)\rangle - \frac{1}{3}\right).$$

3 Interaction between two cortical actin layers

We now solve the equations in the one-dimensional case, considering that the problem is invariant in the x direction. We also look for stationary solutions. The equations governing the gel fluid flow and the gel density are then easily obtained from eqs. (6)

$$\begin{cases} \partial_z(\rho v) = -k_d(\rho - \rho_\infty), \\ 2\eta \partial_{zz} v - \partial_z \Pi(\rho) = 0, \end{cases} \quad (7)$$

where $\Pi(\rho)$ is considered in this section to be a function of ρ only. We do not consider here contributions to the effective pressure involving the derivative of ρ, or higher order derivatives. Such contributions could account for a surface tension between the layer and the solvent.

3.1 Analytic solution of the bilayer problem

We look for a solution on the half-domain $[-\frac{L}{2}, 0]$ and deduce the solution on the other half by symmetry. In this half-domain, the boundary conditions are

$$\rho\big|_{z=-L/2} = \rho_0, \qquad v\big|_{z=-L/2} = v_p, \qquad v\big|_{z=0} = 0.$$

The two first conditions are required by the polymerization at the membrane surface and the last one is required by symmetry. Symmetry could also impose, *a priori*, that $\frac{\mathrm{d}\rho}{\mathrm{d}z}|_{z=0} = 0$. In the following analytical derivation, we find solutions on the half-plane that verify $\frac{\mathrm{d}\rho}{\mathrm{d}z}|_{z=0^-} = -\infty$. These solutions are still symmetric, but the derivative of ρ is not well defined at $z = 0$. There is no mathematical contradiction, since eqs. (7) do not allow to conclude on the continuity of the derivative of ρ near points where the velocity field vanishes.

We integrate the second line of eqs. (7) with respect to z and evaluate the integration constant by using the boundary conditions in $z = 0$. This yields $2\eta\partial_z v = \Pi(\rho) - 2\eta k_d(1 - \frac{\rho_\infty}{\rho_c}) - \Pi(\rho_c)$, where $\rho_c = \rho(z = 0)$ is the density at the center of the domain to be determined. We then define $f(\rho, \rho_c) = g(\rho) - g(\rho_c)$ with $g(\rho) = -\Pi(\rho) + 2\eta k_d(\frac{\rho_\infty}{\rho})$, such that

$$2\eta v = \left(\frac{\mathrm{d}\rho}{\mathrm{d}z}\right)^{-1} \rho f(\rho, \rho_c). \quad (8)$$

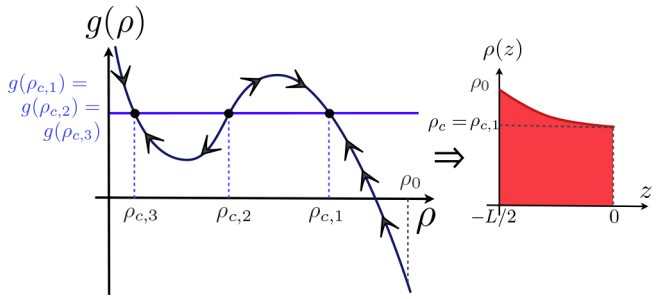

Fig. 3. Schematic of the graphical construction of a solution $\rho(z)$. On the left-hand side graph, the effective gel tension $g(\rho)$ is drawn. According to the position of the curve of $g(\rho)$ to the horizontal line, we deduce the sign of $f(\rho, \rho_{c,1}) = g(\rho) - g(\rho_{c,1\ldots3})$. This allows (eq. (9)) to draw arrows indicating the evolution of ρ as a function of z. If $\rho(z = -L/2) = \rho_0$, then $\rho(z)$ decreases until $\rho_{c,1}$ in $z = 0$, as reported on the right-hand side graph.

We call $g(\rho)$ the effective gel tension[1]. Finally, using eq. (8) and integrating the first line of eqs. (7) yields

$$\frac{\mathrm{d}\rho}{\mathrm{d}z} = \frac{\rho^2 f(\rho, \rho_c)}{2\rho_0 \eta v_p} \exp\left(\int_{\rho_0}^{\rho} \frac{2\eta k_d(\rho' - \rho_\infty)}{(\rho')^2 f(\rho', \rho_c)} \mathrm{d}\rho'\right). \quad (9)$$

The study of the zeros of $f(\rho, \rho_c)$ is essential to find the values of the density to which the profile converges at $z = 0$. Equation (9) indicates that ρ converges to the root of $f(\rho, \rho_c)$, with negative slope, closest to ρ_0. This is not straightforward, and to make the argument clearer, we detail briefly the construction of one solution, with the help of the schematic of fig. 3. We pick three values $\rho_{c,1}$, $\rho_{c,2}$ and $\rho_{c,3}$ that are such that $g(\rho_{c,1}) = g(\rho_{c,2}) = g(\rho_{c,3})$ and $\rho_{c,1\ldots3} \leq \rho_0$. We try to build up the profile $\rho(z)$ and in particular the value of $\rho(z = 0)$. We look first for the sign of $f(\rho, \rho_{c,1\ldots3}) = g(\rho) - g(\rho_{c,1\ldots3})$. If $g(\rho) \leq g(\rho_{c,1\ldots3})$ on an interval, then f is negative on that interval and from eq. (9), we deduce that $\rho(z)$ is a decreasing function of z, and vice versa. This means that the intersections between $g(\rho)$ and $g(\rho_{c,1\ldots3})$ with negative (respectively, positive) slopes give stable (respectively, unstable) fixed points of the density profile. Thus, if we start with $\rho(z = -L/2) = \rho_0$ as in fig. 3, $\rho(z)$ decreases until $\rho(z = 0) = \rho_{c,1}$, and cannot become smaller. To conclude the only possible value of ρ_c is the closest stable fixed point to ρ_0.

The boundary condition: $v|_{z=0} = 0$ must also be satisfied. Combining eqs. (8) and (9) in $z = 0$ yields the condition $\rho_c \geq \rho_\infty$. We consider the experimentally relevant case for which the polymerization in the vicinity of the surface is more efficient than in the bulk, and assume $\rho_0 \geq \rho_\infty$. Knowing from eq. (9) that ρ is a monotonous function of z, we deduce for all z, $\rho(z) \geq \rho_\infty$.

Finally, to compute the value of the density at the midplane ρ_c as a function of the thickness L, we integrate eq. (9) and use the fact that $\rho|_{z=-L/2} = \rho_0$ to obtain the implicit relation

$$\frac{L(\rho_c)k_d}{2v_p} = \int_{\rho_0}^{\rho_c} \frac{2\eta k_d \rho_0}{\rho^2 f(\rho, \rho_c)} \times \ldots \exp\left(-\int_{\rho_0}^{\rho} \frac{2\eta k_d(\rho' - \rho_\infty)}{(\rho')^2 f(\rho', \rho_c)} \mathrm{d}\rho'\right) \mathrm{d}\rho. \quad (10)$$

[1] Not to be confused with the stress in the system.

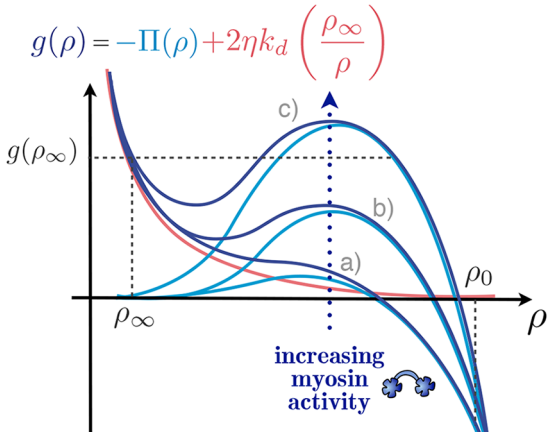

Fig. 4. Dark blue: schematic of the possible shapes of the effective gel tension g according to the contractile properties of the gel. Red: contribution to g associated with depolymerization. Light blue: contribution to g associated with pressure and activity. The cases elaborated in the paper are distinguished: a) *weakly contractile limit*, b) *intermediate contractile limit* and c) *strongly contractile limit*.

3.2 Dependence of the concentration profile on actomyosin contractility

We now emphasize the contributions of two very different terms in the effective gel tension. The contribution of polymerization ($+2\eta k_d \rho_\infty/\rho$) is well known: it is a decreasing function that can be more or less important according to the value of $k_p = k_d \rho_\infty$. The part associated with pressure and activity ($-\Pi(\rho)$) is increasing for small values of ρ (due to myosin activity that is responsible for gel contractility) and then decreasing for higher values of ρ. According to the ratio of $k_d \rho_\infty$ to contractility, g can only have two possible shapes. If the contractility is weak (or $k_d \rho_\infty$ is high), the resulting profile is a monotonous decreasing function (curve (a) of fig. 4). If the contractility is strong (or $k_d \rho_\infty$ is low), the resulting profile has one local minimum and one local maximum (curves (b) and (c) of fig. 4). This results in a strong difference in terms of possible actin density profiles for a given thickness L.

In each limit, two regimes of merging between the two cortical layers are possible. The regime where ρ_c is close to ρ_∞ corresponds to a situation where the layers are separated, and do not interact. We call this regime the *cortical regime*, because the layers are condensed near the surface as the actin cortex [5]. The regime where ρ_c is close to ρ_0 corresponds to a situation where the layers merge and strongly interact. We call this regime the *single*

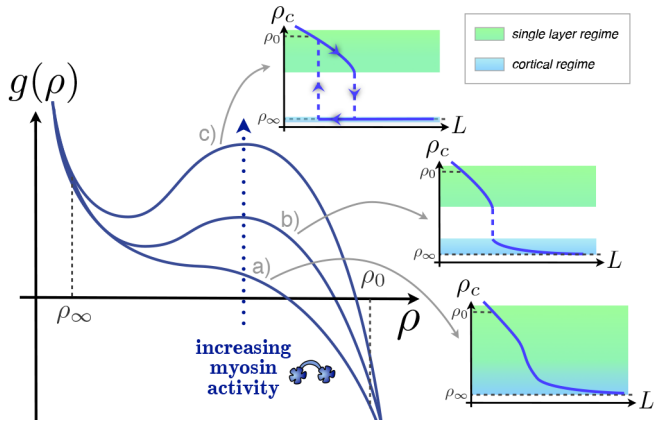

Fig. 5. Left: Schematic of the possible shapes of the effective gel tension g for increasing contractile properties, *e.g.* myosin activity. Right: Associated diagrams of ρ_c, density at the center of the layers, as a function of L, distance between the layers, in different limits: a) *weakly contractile limit*, b) *intermediate contractile limit* and c) *strongly contractile limit*.

layer regime. Because this solution is topologically similar to the actin density located in the *lamellipodium* where only a single dense actin layer may be observed, our study could be a starting point for the study of the transition of the acto-myosin gel from the cortex to the *lamellipodium*. In the subsequent subsection we show the following results:

- In the *weakly contractile limit* there is no clear distinction between the *cortical* and *single layer* regimes. As the layers are brought closer together, the density of actin increases continuously at the center (see inset (a) of fig. 5).
- In the *intermediate contractile limit* g presents a local maximum, which is not larger than $g(\rho_\infty)$ (curve (b) of fig. 4). In this limit, a range of values are not accessible for ρ_c. When the layers are brought closer together, the density at the center of the domain has a sudden jump at a distance L (see inset (b) of fig. 5). There is in this limit a clear distinction between the *cortical* and the *single layer* regimes.
- The *strongly contractile limit* corresponds to even higher contractility, where g presents a local maximum that exceeds the value of $g(\rho_\infty)$ (curve (c) of fig. 4). In this limit, there is hysteresis in the merging of the layers. At large distances, the layers are well separated in the sense that they have a finite thickness smaller than $L/2$. At a distance equal to twice the thickness of a free layer, the layers start interacting. When streched apart the layers do not split in two cortex-like layers until a membrane separation distance significantly larger than twice that of a free layer is reached (see inset (c) of fig. 5).

3.3 Graphical solution

The analytical form of L given by eq. (10) is not very convenient. Indeed, it does not allow to answer explicitly the question of finding the actin density profile (represented by ρ_c) for any value of the spacing between membranes L, since ρ_c is only implicitly expressed in eq. (10). In pratice we eventually fix ρ_c to find L and revert to the more natural relation of ρ_c as a function of L.

Equation (10) allows to derive a few useful results (see appendix B for the derivation):

- *L is a continuous function of ρ_c*. This does not mean however that when the distance between membranes varies, the corresponding evolution of the density profile of actin at the midplane ρ_c is smooth. For instance in the *intermediate* and *strongly* contractile limit, ρ_c is not a smooth function of L (see the insets of fig. 5).
- *L is a decreasing function of ρ_c*. Intuitively, a higher density of actin at the center is more easily achieved when the membranes are closer together.
- *As L goes to 0, ρ_c diverges to $+\infty$*. No limiting value for ρ_c is indeed expected, given that for small L, the total amount of actin filaments is finite, being permanently fed by the surfaces.
- *As L goes to $+\infty$, ρ_c converges to ρ_∞*. Indeed, when the membranes are far apart from each other, the layers interact less, and the density at the midplane approaches that of the free gel.
- *The distance between membranes L_0 to get a uniform density profile*, or $\rho_c = \rho_0$, verifies $\frac{L_0 k_d}{v_p} = \frac{2\rho_0}{\rho_0 - \rho_\infty}$. As a consequence of the second item, as soon as $L \geq L_0$, the density at the center is smaller than ρ_0. For $L \leq L_0$, the membranes are so close that $\rho_c \geq \rho_0$.

The first four results warrant the existence of at least one solution for any value of L.

Furthermore, we notice that eqs. (7) guarantee the continuity of v and ρv as functions of z. The continuity of $\rho(z)$ is not ensured however, in particular if v vanishes, which is the case at least at the midplane. In appendix C we show the following result concerning the condition for the existence of a discontinuity in the profile of $\rho(z)$:

- *The only possible discontinuity in the profile of $\rho(z)$ is between ρ_f and ρ_∞, where ρ_f is the solution to the problem*

$$\begin{cases} g(\rho_f) = g(\rho_\infty) \\ g'(\rho_f) \leq 0 \\ \rho_f \neq \rho_\infty \end{cases} \tag{11}$$

We plot for clarity the construction of this solution in fig. 6.

Such a solution is possible if the effective gel tension g has a local maximum higher than $g(\rho_\infty)$, *e.g.* in the strongly contractile limit. This particular solution corresponds to *free* layers, in the sense that each layer has a

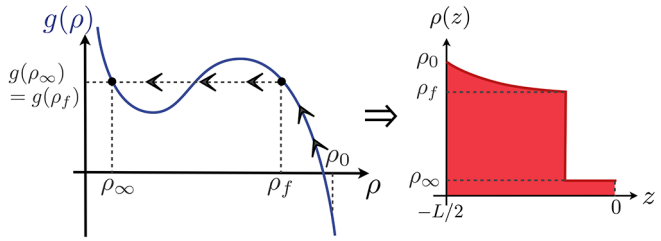

Fig. 6. Schematic of the graphical construction of the solution $\rho(z)$ with a discontinuity in ρ_f as defined by eq. (11). On the left-hand side graph, the effective gel tension $g(\rho)$ is drawn and a graphical construction similar to the one done in fig. 3 is performed. On the right-hand side, the profile $\rho(z)$ with a discontinuity from ρ_f to ρ_∞ is plotted.

finite width corresponding to the part of the density profile that goes from ρ_0 at the membrane to ρ_f. The region where $\rho(z) = \rho_\infty$ can have any width from zero to infinity, allowing to match any distance between membranes larger than $L(\rho_f)$.

These rules of evolution of L with ρ_c allow to build up a plot of L *versus* ρ_c. For a given value ρ_0, we simply look at the function $g(\rho)$. The density profile evolves from ρ_0 to all nearest possible stable fixed points (*e.g.* points where g has a negative slope), which define all values of ρ_c. The corresponding values of L are deduced from the rules.

For simplicity we take in the following a value of ρ_0 rather high, in the sense that it is higher than any relevant variation of the effective gel tension g. The results below can however be easily extended to smaller values of ρ_0.

We conclude now on the solutions of the bilayer problem for the different limits of contractility.

3.3.1 Weakly contractile limit

In the weakly contractile limit, the effective gel tension g is a monotonously decreasing function of ρ (see curve (a) of fig. 4). We start out with $L = L_0$ and thus $\rho_c = \rho_0$. All values of $\rho_c \leq \rho_0$ can be directly reached. ρ_c is thus a continuous decreasing function of L in this case (see fig. 7).

We check our results numerically by simulating a very slow variation of the distance between membranes. A sufficiently slow displacement allows to approach the steady state solutions of the problem. In the numerical solution, we must specify the functional $\Pi(\rho)$. We choose $\Pi(\rho) = a\rho^3 + b\rho^4$ as in [5], where $a < 0$ represents the contractility of the gel and $b > 0$ is a high density coefficient. The cubic power represents the contractile interaction of two actin filaments and one myosin motor (supposed to be present in the gel with a density proportional to that of the actin filaments). We give in appendix D further details on the numerical scheme. In fig. 7 we present both the analytic variation of ρ_c with L and the numerical values obtained at different times as we simulate the displacement of the membranes. The two curves are in perfect agreement. We also show three density profiles to illustrate the transition between the *single layer* (left-hand side) and *cortical regime* (right-hand side).

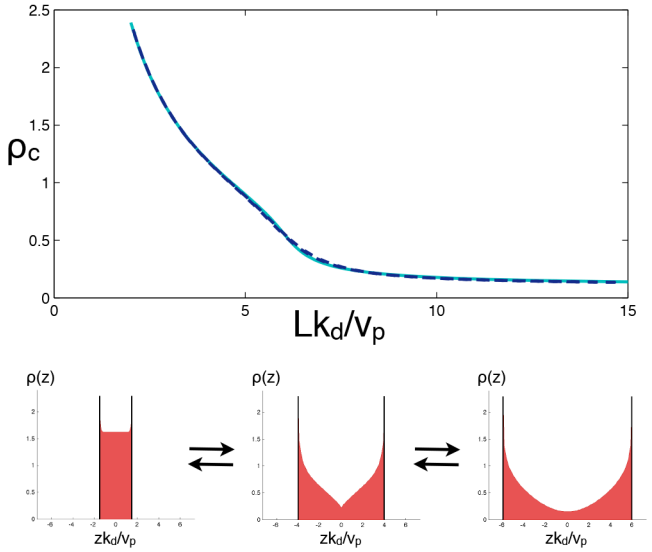

Fig. 7. Top: Evolution of ρ_c as a function of Lk_d/v_p in the weakly contractile limit. The solid light blue line is an analytic integration of L from eq. (10). The dashed dark blue line corresponds to the reported density at the midplane ρ_c during the numerical simulation where L is varied continuously. The parameters are $a = -1\eta k_d$, $b = 2\eta k_d$, $\rho_\infty = 0.1$, $\rho_0 = 2.3$. Bottom: Density profiles chosen from the numerical simulation, for $Lk_d/v_p = 3, 8, 12$ from left to right. The black vertical lines in each density profile represent the membranes.

3.3.2 Intermediate contractile limit

In the intermediate contractile limit, the effective gel tension g has one local minimum and one local maximum. We recall that $g(\rho_{\mathrm{loc\,max}}) \leq g(\rho_\infty)$, where $g(\rho_{\mathrm{loc\,max}})$ is the value of g at the local maximum.

We start out with $L = L_0$ and $\rho_c = \rho_0$ and construct solutions from ρ_0 to smaller and smaller values of ρ_c, and larger and larger values of L, until $\rho_{\mathrm{loc\,max}}$. At that point, $L = L_c^+$. If we want to go on decreasing ρ_c, the only solution is for ρ_c to jump to the other value ρ_{jump} that verifies $g(\rho_{\mathrm{jump}}) = g(\rho_{\mathrm{loc\,max}})$. At that other point, $L = L_c^-$. Afterwards, we may go on decreasing ρ_c until ρ_∞, with L increasing continuously.

This raises the question of the existence of a solution for any L, in other words whether $L_c^- = L_c^+$. We use the expression of $L(\rho_c)$ of eq. (10) and recall that $g(\rho_{\mathrm{loc\,max}}) = g(\rho_{\mathrm{jump}})$. Writing $L_c^- - L_c^+ = L(\rho_{\mathrm{jump}}) - L(\rho_{\mathrm{loc\,max}})$ yields the integral of a function that always vanishes, so that $L_c^- = L_c^+ = L_c$.

In summary, we have found, in the intermediate contractile limit, that the distinction between the *cortical* and the *single layer regime* is clearly characterized by a critical length between membranes L_c.

In the same way as for the weakly contractile limit, we check our results numerically by simulating a very slow displacement of the membranes. We take a larger value of a in absolute value than for the weakly contractile limit (the contractile properties are thus enhanced). In fig. 8 we present both the analytic variation of ρ_c with L and the

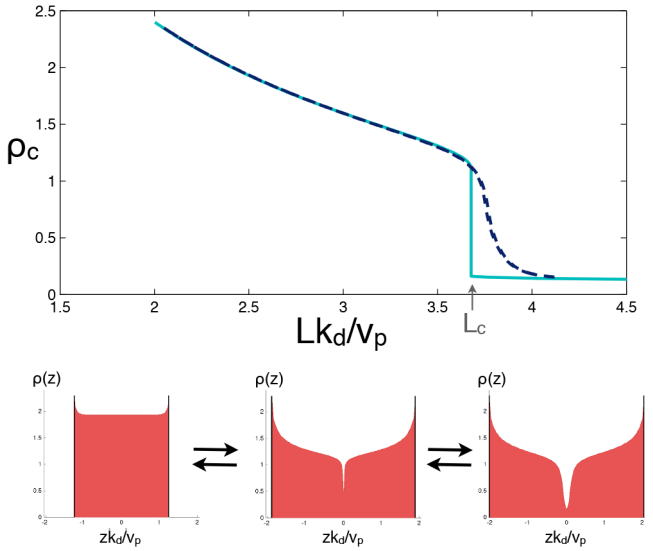

Fig. 8. Top: Evolution of ρ_c as a function of Lk_d/v_p in the intermediate contractile limit. The solid light blue line is an analytic integration of L from eq. (10). The dashed dark blue line corresponds to the reported density at the midplane ρ_c during the numerical simulation where L is varied continuously. The parameters used are $a = -3\eta k_d$, $b = 2\eta k_d$, $\rho_\infty = 0.1$, $\rho_0 = 2.3$. Bottom: Density profiles chosen from the numerical simulation, for $Lk_d/v_p = 2.5, 3.8, 4.1$ from left to right. The black vertical lines in each density profile represent the membranes.

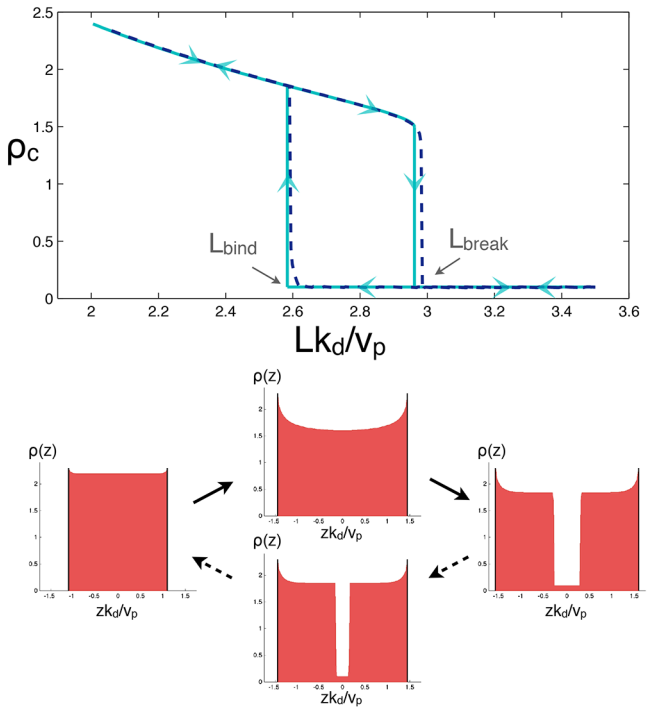

Fig. 9. Top: Evolution of ρ_c as a function of Lk_d/v_p in the strongly contractile limit. The solid light blue line is an analytic integration of L from eq. (10). The dashed dark blue line corresponds to the reported density at the midplane ρ_c during the numerical simulation where L is varied continuously. The parameters are $a = -4\eta k_d$, $b = 2\eta k_d$, $\rho_\infty = 0.1$, $\rho_0 = 2.3$. Bottom: Density profiles chosen from the numerical simulation, for $Lk_d/v_p = 2.2, 2.9, 3.2$ from left to right. The black vertical lines in each density profile represent the membranes. The profile for $Lk_d/v_p = 2.9$ is plotted in the case of layers being stretched apart (right solid arrows) and being pushed together (left dashed arrows).

numerical calculation *versus* time as we simulate the displacement of the membranes. Both variations are in close agreement. Near the critical length L_c, the numerical calculation (dashed line) demonstrates smoother variations than the analytical profile. This is due to the finite displacement speed of the membranes.

3.3.3 Strongly contractile limit

Single layer and cortical regimes

We now focus on the strongly contractile limit. The profile of the effective gel tension g has a local minimum and a local maximum as before, but the contractile pressure contribution to g is very important, *e.g.* $g(\rho_{\mathrm{loc\,max}}) \geq g(\rho_\infty)$. The construction of the variations of L as a function of ρ_c starts as above. As L increases, ρ_c gets closer to $\rho_{\mathrm{loc\,max}}$. At this particular point, we try to find some stable value of $\rho_c \leq \rho_{\mathrm{loc\,max}}$ and such that $g(\rho_c) \geq g(\rho_{\mathrm{loc\,max}})$. This leads to $\rho_c \leq \rho_\infty$ which we have demonstrated to be impossible (in that limit the velocity field at the center is infinite). We denote the distance at which the layers can no longer be merged $L_{\mathrm{break}} = L(\rho_{\mathrm{loc\,max}})$.

We call $L_{\mathrm{bind}} = L(\rho_f)$ the critical length for which the separated layers (solution with discontinuous density mentioned in eq. (11)) barely touch. L_{bind} corresponds to twice the width of the single free layer. From eq. (11) we have $\rho_f \geq \rho_{\mathrm{loc\,max}}$, and as $L(\rho_c)$ is a decreasing function of ρ_c we easily get $L_{\mathrm{bind}} \leq L_{\mathrm{break}}$.

This reasoning demonstrates the existence of two solutions for lengths L in the interval $[L_{\mathrm{bind}}, L_{\mathrm{break}}]$. One solution corresponds to the *cortical* regime with sharp delimited layers and $\rho_c = \rho_\infty$. The other solution corresponds to merged layers, with $\rho_c > \rho_\infty$. It is the *single layer* regime. For $L \leq L_{\mathrm{bind}}$ the layers are merged. For $L \geq L_{\mathrm{break}}$ the layers are clearly separated.

Hysteresis effects

In order to determine in which regime the layers are for a given L in the critical interval $[L_{\mathrm{bind}}, L_{\mathrm{break}}]$, one must rely on the history of the double layer.

We consider the thought experiment of two *cortical* layers well separated and far apart. Infinitesimally slowly, the membranes are moved closer to one another. If fluctuations are small, the layers stay separated until $L = L_{\mathrm{bind}}$. At this critical length, they merge, the density at the center jumps from ρ_∞ to ρ_f. The system is now a *single layer*. As the membranes are moved closer still, the density at the center increases continuously. Upon moving the membranes apart the density at the center continuously decreases. For $L = L_{\mathrm{bind}}$, the density at the center is ρ_f. Pulling the membranes further apart, the *single layer*

starts to stretch, and the density at the center continues to decrease. At some critical point, where $\rho_c = \rho_{\mathrm{loc\,max}}$, and $L = L_{\mathrm{break}}$ the layer breaks apart and forms two well separated layers again, relaxing in the *cortical* regime.

This is well reproduced numerically, as illustrated in fig. 9. The analytic integration of eq. (10) and the numerical simulation are in close agreement, and demonstrate the hysteresis phenomenon between L_{bind} and L_{break}. Near these critical lengths, the numerical curve (dashed line) shows again smoother variations than the analytic profile. This is again due to the finite displacement speed of the membranes. We also present in fig. 9 density profiles to illustrate the transition with hysteresis from *single layer* (on the left-hand side) to *cortical* regime (on the right-hand side).

4 Stability of a stretched single layer

The coexistence of two regimes in the strongly contractile limit leads to the question of their relative stability. In this section, we study the stability of the stretched *single layer*. The general methodology for the study of the stability of the solutions is a linear expansion for small perturbations. Here this expansion is difficult and cannot lead to a simple answer because the system reacts very differently to a small addition or removal of matter. Indeed, numerically, it is easy to observe that an addition of matter on a stretched *single layer* leaves it intact. On the contrary, a removal of matter may damage the merged configuration irreversibly and the system relaxes to two separate *cortical* layers.

That explains why we choose to study the stability of the stretched *single layer* solutions in the following way: we study numerically the impact of a small removal of matter at the center of the domain, which respects the symmetry of the steady state solution.

4.1 Qualitative discussion of stability

We perform the following "numerical experiment". The initial condition is a stretched *single layer* steady state profile, into which a "hole" is introduced by lowering locally the density at the midplane. The hole depth ε is varied (in units of concentration). The width of the hole is chosen so that the hole is not too thin, but never wider than the space between the layers of the separate regime at $L = L_{\mathrm{break}}$. The width of the hole is not varied, and we checked that it has little impact on the final result. We study the effect of the removal for various values of $L \in [L_{\mathrm{break}}, L_{\mathrm{bind}})$.

This allows to draw a stability diagram for the stretched layer in the plane L *versus* damage depth ε, as shown in fig. 10. As expected, the more stretched the *single layer*, the smaller the critical depth to break apart the layer. As the layer is stretched up to $L = L_{\mathrm{break}}$, almost any removal depth breaks the *single layer* into two separated layers.

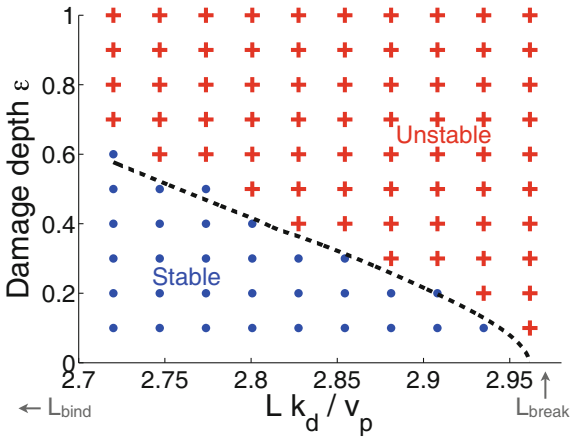

Fig. 10. Stability of the stretched layer as a function of the spacing between membranes (Lk_d/v_p) and the depth of the hole performed (ε). Each numerical experiment is represented by a data point. Red crosses represent coordinates that are unstable with respect to such a removal (*e.g.* the *single layer* breaks apart), blue spots represent coordinates that are stable. The dashed black line represents the analytical condition discussed in the text and corresponding to $\Pi(\rho_c(L) - \varepsilon) = \Pi(\rho_c(L))$. It ensures that all points below the line are stable. The numerical parameters used are the same as in fig. 9.

An interpretation of these results is based on the consideration of the initial velocity profile, just after the perturbation of the concentration profile. Let the velocity field be written as $v(z,t) = v_s(z) + w(z,t)$ where $v_s(z)$ is the steady state solution, and $w(z,t)$ the time-dependent correction to the steady state. In the same way we write $\rho(z,t) = \rho_s(z) + \delta\rho(z,t)$. With these notations the stress balance from eqs. (7) reads

$$2\eta\partial_{zz}w(z,t) = \partial_z\Pi(\rho_s(z) + \delta\rho(z,t)) - \partial_z\Pi(\rho_s(z)). \tag{12}$$

Equation (12) yields, at time $t = 0$, a good intuition of the initial velocity field induced by the perturbation.

We assume for simplicity that the hole in the concentration profile is performed roughly on a domain where $\rho_s(z) \simeq \rho_c$. On that interval $\delta\rho(z,0) = -\varepsilon$ with $\varepsilon > 0$. Away from the hole, $\delta\rho(z,0) = 0$. We remind also the boundary conditions on $w(z,0)$: $w(-L/2,0) = w(0,0) = w(L/2,0) = 0$.

Near the stability limit of the *single layer* ($\rho_{\mathrm{loc\,max}}$), the effective pressure as a function of ρ has a minimum. Therefore, $\Pi(\rho_c - \varepsilon)$ can either be greater or smaller than $\Pi(\rho_c)$. For instance, if ε is small and that we are far enough from $\rho_{\mathrm{loc\,max}}$, we have $\Pi(\rho_c - \varepsilon) \leq \Pi(\rho_c)$. Then, from eq. (12) the velocity field $w(z,0)$ is positive for $z < 0$ and negative for $z > 0$. This actin flow thus contributes to the healing of the layer, by filling up the initial hole. If, on the contrary, ε is large and that we are close to the concentration $\rho_{\mathrm{loc\,max}}$, *e.g.* close to the breaking point of the *single layer*, $\Pi(\rho_c - \varepsilon) > \Pi(\rho_c)$. Then, the resulting actin flow $w(z,0)$ from eq. (12) contributes to the breaking of the layer.

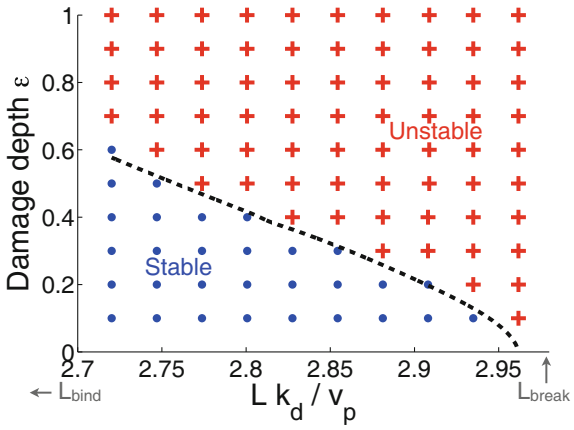

Fig. 11. Stability of the stretched layer as a function of the spacing between membranes (Lk_d/v_p) and the depth of the hole performed (ε) for a two-dimensional geometry with isotropic contractile properties. Each numerical experiment is represented by a data point. Red crosses represent coordinates that are unstable with respect to a removal of matter, blue spots represent coordinates that are stable. The dashed black line represents the analytical condition for stability in 1D discussed in the text. It is reported from fig. 10. The numerical parameters used are the same as for fig. 9 with specifically $a = a' = -4\eta k_d$.

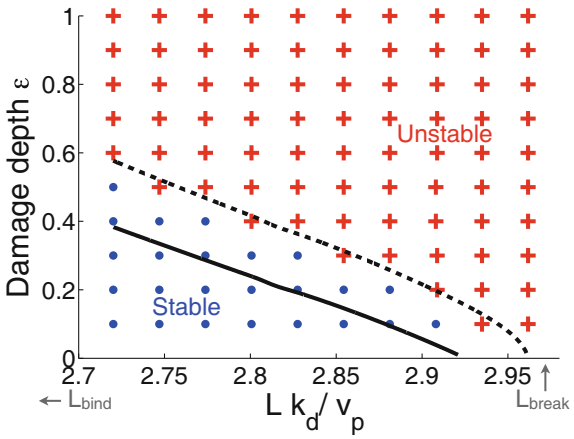

Fig. 12. Stability of the stretched layer as a function of the spacing between membranes (Lk_d/v_p) and the depth of the hole performed (ε) for a two-dimensional geometry with anisotropic contractile properties. Each numerical experiment is represented by a data point. Red crosses represent coordinates that are unstable with respect to a removal of matter, blue spots represent coordinates that are stable. The dashed black line represents the analytic condition for stability in 1D discussed in the text. The solid black line represents the 2D extension of this condition. It ensures that all points below the line are stable. The numerical parameters used are the same as for fig. 9 with specifically $a = -4\eta k_d$ and $a' = -4.2\eta k_d$.

One must however consider the total velocity field at the initial time $v(z,0) = v_s(z) + w(z,0)$ where the steady state flow $v_s(z)$ always contributes to the healing of the layer. The condition of monotonous increase of the pressure is therefore only a sufficient condition for the healing of the layer. The limit $\Pi(\rho_c - \varepsilon) = \Pi(\rho_c)$ is reported on fig. 10 as a dashed black line. On fig. 10 we verify that all points beneath the line are stable. All points above the line are not unstable: those closest to the line are still stable. Altogether this analytical condition yields an interesting intuition on the reasons for stability. The stability of the layer is closely related to the contractility of the gel.

4.2 Two-dimensional anisotropy

We recall from eqs. (6) that the actin layer in two dimensions has anisotropic contractile properties. Because contractility is essential in the study of stability, we study here the two-dimensional extension of the problem. Numerical solutions require the expressions for the functions $\Pi_x(\rho)$ and $\Pi_z(\rho)$. We write $\Pi_z(\rho) = a\rho^3 + b\rho^4$ as in the one-dimensional case, and choose $\Pi_x(\rho) = a'\rho^3 + b\rho^4$, where $a' < 0$ can be different from a and characterizes the contractile properties in the x direction.

For completeness we study first the case of isotropic contractility, *e.g.* $a = a'$ (this corresponds to an isotropic distribution of the orientation of filaments θ in eq. (1)). We perform the same "experiments" as in one dimension, studying the evolution of a rectangular shaped hole in the concentration profile at the center of the domain. Only the depth of the hole is varied, keeping the width constant as in the one-dimensional case, as well as the length in the x direction, parallel to the membranes. We also checked that this parameter has little influence on the results.

The results for isotropic contractility are summarized in fig. 11. As expected, the simulations prove to be fairly comparable to the one-dimensional case. On fig. 11, only one data point ($Lk_d/v_p = 2.77$ and a hole depth of 0.5) differs from the one-dimensional case, which is unstable whereas it is stable in one dimension. This difference has little relevance on the global aspect of the diagram. Moreover, the analytical condition for the one-dimensional case, reported on fig. 11, remains a good indicator for the stability of the stretched solutions.

We now perform the same "experiments" in the case of anisotropic contractility. Phenomenologically we expect contractility to be larger in the plane parallel to the main filament direction than in the direction perpendicular. In the *single layer*, where the membranes are closely facing each other, we expect the filaments to be mainly parallel to the plane of the membranes (x, y plane). In eq. (1), this can be coarsely modeled by setting $\theta \equiv \pi/2$. This yields $\zeta_x - \zeta_z = \zeta'/2 < 0$ in eqs. (6), and $a' < a$, that we expected.

We summarize the results in fig. 12. We observe that the increased contractility in the x direction results in the extension of the unstable domain. The former condition on Π obtained in the one-dimensional case, represented by the dashed black line on fig. 12, stipulating that all points below the line are stable, is no longer valid. This is because the condition only considers Π_z, and takes into account only the coefficient a, *e.g.* only the contractile

activity perpendicular to the membranes. Since $a' < a$, to write a valid analytical condition, we must now apply the same reasoning as in subsect. 4.1 for the velocity u in the x direction. We obtain that the stability of the layer is insured if $\Pi_x(\rho_c - \varepsilon) \leq \Pi_x(\rho_c)$ and $\Pi_z(\rho_c - \varepsilon) \leq \Pi_z(\rho_c)$. The combined conditions yield the new solid black line in fig. 12. This sufficient condition for stability is well verified: all points beneath the solid line are stable points.

We conclude that an excess contractility in the tangential direction destabilizes the stretched *single layer*.

On the other hand, if the filaments are mainly aligned with the direction z, perpendicular to the membranes, contractility is more important in that direction compared to the x, y directions. This writes $a < a'$. Lowered contractility in the tangential direction would then stabilize the stretched *single layer*.

5 Discussion

In this paper we have applied the theory of active gels to investigate the merging of two cortical actin layers into a single dense layer, similar in that way to the *lamellipodium*. We have shown that the activity of the actomyosin gel is essential for the understanding of the merging mechanism. Our main result is that a gel with strong contractility shows hysteresis in the merging of the two cortical layers. The transition from the single dense layer to two separate layers of actin cortex happens through a stretched configuration of the single layer. This stretched configuration has interesting stability properties, also monitored by contractility. As expected the more stretched the single layer, the less it is stable. In addition, an excess contractility in the tangential direction, due to alignment of the actin filaments along the membranes, is a source of instability of the stretched single layer.

In this study we did not consider the effect of actin density gradients in the effective pressure for simplicity. We do not expect that such terms play a major role in the physics we presented. It is easy to verify that the addition of a term proportional to $\nabla^2\rho$ in the effective pressure smoothens steep concentration profiles and suppresses the artificial jumps in concentration that we found here. It does not affect either the key role of contractility or the hysteresis phenomenon. On stretched one-dimensional solutions, it also has a stabilizing effect. This is interesting because it could balance the destabilizing effect of tangential contractility in two-dimensions. It is also of physical relevance because such a term could account for surface tension between the gel and the solvent.

Another limitation of our work is that we did not consider in details the orientation of the actin filaments. We have imposed that they are either parallel to the membrane with no preferred direction in the tangential plane, or isotropically distributed. A more complete theory will have to consider an orientation profile of the actin filaments that is coupled to the concentration and velocity profiles. For instance, in the study of the healing of a wounded stretched *single layer*, one should consider the variations of filament orientation around the wound. Neglecting such variations is only possible when the elastic modulus anisotropy is small. Here also, we do not expect any qualitative changes in the results.

The assumption of symmetric conditions of actin polymerization on each membrane can also be discussed. The cortex images of fig. 1(c) and (d) seem to indicate that the layer attached to the substrate and the layer attached to the "free" membrane have different thicknesses, although the precise trend is unclear. Asymmetric boundary conditions on the one-dimensional problem can be treated in a similar way as the symmetric boundary conditions. Because actin is polymerizing from each side, and because the velocity of the gel is a continuous function of z, the velocity has to vanish at a point z_0, which is no longer the middle of the actin slab. At this point however the density is still continuous, and we can redefine $\rho_c = \rho(z_0)$. The graphical construction can then be conducted on each side, in the same way as was done in sect. 3.3. For high actomyosin activities, the layers can bind at a distance equal to the sum of their respective free layer widths. When stretched again, they will separate at a larger distance. The hysteresis predicted for the symmetric case should also exist in the asymmetric one.

Several extensions of this work are possible. An important one would be to go beyond the steady state and consider the kinetics of formation of merging of two cortical layers. This requires the solution of the time-dependent equations for the cortical layers and is left for future work. Contractile waves are also often observed in cells [10] and it would be interesting to investigate their existence within the framework of our model.

Our predictions could be tested experimentally in different ways, not only to test the hysteretic behavior of the acto-myosin gel but also to confirm that the theory of active gels is able to describe in particular the acto-myosin gel. Pulling the upper membrane of a cell fragment with a well-defined surface and recording the force to pull and push it would allow a direct visualization of the hysteretic behavior of attachment of the actin layers. One could also confine cells between parallel plates monitoring carefully their separation and measuring the actin density profile as a function of thickness. It would also be of interest to track by fluorescence the actin distribution over time in moving cells, especially at the separation point. In any of these experiments, acto-myosin contractility could be increased or decreased using for instance myosin activators or inhibitors.

Other extensions of the theory could aim at a more realistic description of the *lamellipodium* in cells, in particular by investigating the height and shape of a cell from the near nucleus region to the edge of the *lamellipodium*. Apart from a possible three-dimensional extension of the theory, this would require writing explicitly force balance equations both perpendicular and parallel to the substrate. It would also require to investigate the longitudinal actin flux, and the variation in the polymerization conditions near the membranes.

Author contribution statement

Several people contributed to the work described in this paper. S.M., J.-F.J., and J.P. conceived the basic idea for this work. S.M. developed the theory and the simulations to identify the mechanisms of attachment of actin layers. A.L.G. and D.R. designed and performed the experiments to visualize *lamellipodia*. J.-F.J. and J.P. supervised the research and, with D.R., helped with the development of the paper.

The authors would like to thank Andrew Callan-Jones for discussions regarding [13]. They also would like to thank Pr. Karsten Kruse for enlightning meetings on the theory of active gels, and Pascal Kessler from IGBMC. They thank Matthieu Piel for useful discussions concerning experimental suggestions to check the predictions of the theory. Finally, they are indebted to Tatyana Svitkina and Günther Gerisch for helpful discussions on the acto-myosin cortex and the *lamellipodium*.

Appendix A. Cell culture and observations

Synthetic polyamines (C8-BPA) were recently shown to promote growth of *lamellipodia* within minutes [20]. In our context, we used them and visualized the cell cortex along the z-axis on single spread cells with different experiments (see fig. 1). Symmetric (fig. 1(c)) and non-symmetric (fig. 1(d)) cells were recorded depending on the experimental conditions. When C8-BPA is added on already spread cells, *lamellipodia* growth is promoted as well, but cortical layers stay non-symmetric around the nucleus.

Mouse NIH3T3 fibroblasts (ATCC, Manassas, VA) were grown in high glucose Dulbecco's Modified Eagle's Medium (Invitrogen, Reims, France) supplemented with 1% Pen Strep antibiotics (Invitrogen, Reims, France) and 10% bovine calf serum (BCS, Sigma-Aldrich, Lyon, France) at 37 °C and 5% CO_2. For symmetric cells, C8-PBA was added 1 hour and 20 min after cell resuspension using trypsin treatment. For non-symmetric cells, C8-BPA (100 μM) was incubated 80 min after seeding or on spread cells for 10 min before fixation with 3% paraformaldehyde (Sigma-Aldrich, France) at 37 °C for 17 min. Then, 0.5% Triton (Sigma-Aldrich, France) was added for 3 min to permeabilise cells, and samples were washed twice for 5 min with 1X PBS. For staining, we used fluorescent phalloidin (Molecular Probes) for F-actin, rabbit anti-myosin IIB (Sigma-Aldrich, France) for myosin with a fluorescent secondary antibody, and DAPI (4.6-diamidino-2-phenylidole, Sigma-Aldrich, France) for the nucleus. Cells were observed on a Leica SP5 inverted microscope with a 63× oil immersion objective (N.A. 1.4). Images were acquired with stacks of x-y planes spanning the cells width with z-step sizes of 0.25 μm. Planes along various directions were reconstructed with Imaris and Image J.

Appendix B. Tools for graphical resolution

In the following we work with adimensional variables such that eq. (10) reduces to

$$L(\rho_c) = 2\int_{\rho_0}^{\rho_c} \frac{\rho_0}{\rho^2(g(\rho)-g(\rho_c))} \times \ldots \exp\left(-\int_{\rho_0}^{\rho} \frac{(\rho'-\rho_\infty)}{(\rho')^2(g(\rho')-g(\rho_c))} d\rho'\right) \mathrm{d}\rho \qquad \text{(B.1)}$$

and show the results of subsect. 3.3.

L is a decreasing function of ρ_c

We calculate L in the vicinity of the midpoint $L(\rho_c(1+\varepsilon))$ and we assume that $\rho_c \geq \rho_0$, and $\varepsilon > 0$. This leads, at $o(\varepsilon)$, to

$$\begin{aligned}
&L(\rho_c(1+\varepsilon)) - L(\rho_c) = \\
&2\int_{\rho_0}^{\rho_c} \frac{\rho_0 \mathrm{d}\rho}{\rho^2(g(\rho)-g(\rho_c))} \exp\left(-\int_{\rho_0}^{\rho} \frac{\rho'-\rho_\infty}{(\rho')^2(g(\rho')-g(\rho_c))} d\rho'\right) \\
&\times \ldots \varepsilon\left[\frac{g'(\rho_c)}{(g(\rho)-g(\rho_c))} - g'(\rho_c)\left(\int_{\rho_0}^{\rho} \frac{\rho'-\rho_\infty}{(\rho')^2(g(\rho')-g(\rho_c))^2} d\rho'\right)\right] \\
&+\int_{\rho_c}^{\rho_c(1+\varepsilon)} \frac{\rho_0 \mathrm{d}\rho}{\rho^2(g(\rho)-g(\rho_c))} \exp\left(-\int_{\rho_0}^{\rho} \frac{\rho'-\rho_\infty}{(\rho')^2(g(\rho')-g(\rho_c))} \mathrm{d}\rho'\right) \\
&\times \ldots \left(1+\varepsilon\left[\frac{g'(\rho_c)}{(g(\rho)-g(\rho_c))} - g'(\rho_c)\left(\int_{\rho_0}^{\rho} \frac{\rho'-\rho_\infty}{(\rho')^2(g(\rho')-g(\rho_c))^2} d\rho'\right)\right]\right).
\end{aligned}$$

There are two integrals to study. We study the first integral and more particularly the function

$$F(\rho) = \frac{g'(\rho_c)}{(g(\rho)-g(\rho_c))} - g'(\rho_c)\left(\int_{\rho_0}^{\rho} \frac{\rho'-\rho_\infty}{(\rho')^2(g(\rho')-g(\rho_c))^2} d\rho'\right).$$

The derivative of this function is

$$F'(\rho) = \frac{(\rho-\rho_\infty)}{(g(\rho)-g(\rho_c))^2}\left[\frac{g'(\rho)(\rho-\rho_\infty)}{\rho^2} - 1\right].$$

In the domains of interest, $g'(\rho)$ is always negative and $\rho \geq \rho_\infty$ such that $F'(\rho) \leq 0$ and $F(\rho) \leq F(\rho_0) \leq 0$. This shows that the first integral can be rewritten as $-\alpha\varepsilon$ with α a positive constant.

We now consider the second integral and perform the change of variables $\rho = \rho_c(1+\epsilon)$. We get

$$\begin{aligned}
&\int_{\rho_c}^{\rho_c(1+\varepsilon)} \frac{\rho_0 \mathrm{d}\rho}{\rho^2(g(\rho)-g(\rho_c))} \exp\left(-\int_{\rho_0}^{\rho} \frac{(\rho'-\rho_\infty)d\rho'}{(\rho')^2(g(\rho')-g(\rho_c))}\right)(1+O(\varepsilon)) \\
&= \int_0^{\varepsilon} \frac{\rho_0 \mathrm{d}\epsilon}{\epsilon\rho_c^2 g'(\rho_c)} \exp\left(-\int_{\frac{\rho_0}{\rho_c}-1}^{\epsilon}\left(\frac{\rho_c-\rho_\infty}{(\rho_c)^2 g'(\rho_c)\epsilon'} + O(1)\right)\mathrm{d}\epsilon'\right)(1+O(\varepsilon)) \\
&= \int_0^{\varepsilon} \frac{\rho_0 \mathrm{d}\epsilon}{\epsilon\rho_c^2 g'(\rho_c)} \exp\left(\frac{-(\rho_c-\rho_\infty)}{(\rho_c)^2 g'(\rho_c)} \ln\left(\frac{\epsilon}{\frac{\rho_0}{\rho_c}-1}\right) + O(\epsilon)\right)(1+O(\varepsilon)) \\
&= \int_0^{\varepsilon} \frac{\rho_0 \mathrm{d}\epsilon}{\rho_c^2 g'(\rho_c)} \exp\left(\frac{\rho_c-\rho_\infty}{(\rho_c)^2 g'(\rho_c)} \ln\left(\frac{\rho_0}{\rho_c}-1\right)\right) \\
&\times \ldots \left(\epsilon^{-1-\frac{\rho_c-\rho_\infty}{(\rho_c)^2 g'(\rho_c)}} + O\left(\epsilon^{-\frac{\rho_c-\rho_\infty}{(\rho_c)^2 g'(\rho_c)}}\right)\right)(1+O(\varepsilon)) \\
&= -\frac{\rho_0}{\rho_c-\rho_\infty} \exp\left(+\left(\frac{\rho_c-\rho_\infty}{(\rho_c)^2 g'(\rho_c)} \ln\left(\frac{\rho_0}{\rho_c}-1\right)\right)\right)\left(\varepsilon^{-\frac{\rho_c-\rho_\infty}{(\rho_c)^2 g'(\rho_c)}}\right) \\
&+O\left(\varepsilon^{-\frac{\rho_c-\rho_\infty}{(\rho_c)^2 g'(\rho_c)}+1} + \varepsilon^2\right).
\end{aligned}$$

With these notations, one sees that the highest-order term in ε contributing to the full second integral of the expansion of $L(\rho_c(1+\varepsilon)) - L(\rho_c)$, is the term

$$-\frac{\rho_0}{\rho_c - \rho_\infty} \exp(\ldots)\varepsilon^{-\frac{\rho_c-\rho_\infty}{(\rho_c)^2 g'(\rho_c)}},$$

which is negative, and that all other terms are at least $O\big(\varepsilon^{-\frac{\rho_c-\rho_\infty}{(\rho_c)^2 g'(\rho_c)}+1} + \varepsilon^2\big)$ so in the end $o(\varepsilon)$.

Finally we get

$$L(\rho_c(1+\varepsilon)) - L(\rho_c) = -\alpha\varepsilon - \beta\varepsilon^{-\frac{\rho_c-\rho_\infty}{(\rho_c)^2 g'(\rho_c)}} + o(\varepsilon),$$

with α and β positive constants. This result imposes that $L(\rho_c(1+\varepsilon)) \leq L(\rho_c)$ and thus that L is a decreasing function of ρ_c.

We performed the above calculations assuming that $\rho_c \geq \rho_0$. However, the principle of the calculation does not change if we assume the reverse and the main result stays identical.

As L goes to $+\infty$, ρ_c converges to ρ_∞

We perform an expansion of L by writing $\rho_c \simeq \rho_\infty(1+\varepsilon)$ where $\varepsilon > 0$.

$$\begin{aligned}
&L(\rho_\infty(1+\varepsilon))\\
&= \int_{\rho_0}^{\rho_\infty(1+\varepsilon)} \frac{\rho_0 \mathrm{d}\rho}{\rho^2(g(\rho)-g(\rho_\infty))} \exp\left(-\int_{\rho_0}^{\rho} \frac{\rho'-\rho_\infty}{(\rho')^2(g(\rho')-g(\rho_\infty))}\mathrm{d}\rho'\right)\\
&= \int_{\frac{\rho_0}{\rho_\infty}-1}^{\varepsilon} \frac{\rho_0 \mathrm{d}\epsilon}{\epsilon\rho_\infty^2 g'(\rho_\infty)} \exp\left(-\int_{\frac{\rho_0}{\rho_\infty}-1}^{\epsilon} \left(\frac{\rho_\infty \epsilon'}{(\rho_\infty)^2 g'(\rho_c)\epsilon'} + O(\epsilon')\right)\mathrm{d}\epsilon'\right)\\
&= \int_{\frac{\rho_0}{\rho_\infty}-1}^{\varepsilon} \frac{\rho_0 \mathrm{d}\epsilon}{\epsilon\rho_\infty^2 g'(\rho_\infty)} \exp\left(-\left(\frac{\rho_\infty}{(\rho_\infty)^2 g'(\rho_c)}\left(\frac{\rho_0}{\rho_\infty}-1\right)\right)\right)(1+O(\epsilon))\\
&= \frac{\rho_0}{\rho_\infty^2 g'(\rho_\infty)} \exp\left(-\left(\frac{\rho_\infty(\rho_0-\rho_\infty)}{(\rho_\infty)^2 g'(\rho_c)\rho_\infty}\right)\right)\ln\left(\frac{\varepsilon}{\frac{\rho_0}{\rho_\infty}-1}\right) + O(\varepsilon).
\end{aligned}$$

Under this form we observe that

$$\lim_{\varepsilon\to 0} L(\rho_\infty(1+\varepsilon)) = +\infty.$$

As L goes to 0, ρ_c diverges to $+\infty$

This result has little physical meaning, since we are not much interested by situations corresponding to $\rho_c \geq \rho_0$, or $L \leq L_0$. However, it is of mathematical interest to verify that we can obtain solutions corresponding to all values of L. For that we integrate the first line of eqs. (7), which yields

$$\frac{2\rho_0 v_p}{L} + \rho_\infty k_d = k_d \frac{1}{L}\int_{-L/2}^{L/2} \rho(z)\mathrm{d}z,$$

such that if we define $\rho_m = \frac{1}{L}\int_{-L/2}^{L/2}\rho(z)\mathrm{d}z$ the average value of $\rho(z)$, ρ_m diverges as $L \to 0$.

Appendix C. Conditions for a discontinuity in the density profile

We first assume that there is at least one point of discontinuity in the density profile. Let z_0 be the closest point to the left-hand side membrane, where a discontinuity happens.

Integrating the first line of eqs. (7) with respect to z between $z_0-\epsilon$ and $z_0+\epsilon$, and taking the limit $\epsilon \to 0$ yields the continuity of flux

$$\rho(z_0)^+ v(z_0)^+ = \rho(z_0)^- v(z_0)^-.$$

Integrating the second line alike yields the continuity of stress

$$2\eta\partial_z v(z_0)^+ - \Pi(\rho(z_0))^+ = 2\eta\partial_z v(z_0)^- - \Pi(\rho(z_0))^-,$$

and integrating the second line twice yields the continuity of the velocity

$$v(z_0)^+ = v(z_0)^-.$$

This last equation, combined with the continuity of flux, tells us that a discontinuity in z_0 is possible if and only if the velocity vanishes in that point

$$v(z_0)^+ = v(z_0)^- = 0.$$

We now look for the density $\rho(z_0)^-$ on the left of the jump. On the interval $[-L/2, z_0)$ we can solve the equations analytically and obtain

$$v\big|_{z=z_0^-} = v_p \frac{\rho_0}{\rho(z_0)^-} \exp\left(-\int_{\rho_0}^{\rho(z_0)^-} \frac{2\eta k_d(\rho'-\rho_\infty)\mathrm{d}\rho'}{(\rho')^2(g(\rho')-g(\rho_c))}\right).$$

The only way to let $v|_{z=z_0-} = 0$ is that $g(\rho(z_0)^-) = g(\rho_c)$. This defines a unique $\rho(z_0)^-$, corresponding to the solution of $g(\rho(z_0)^-) = g(\rho_c)$, with $\rho(z_0)^- \geq \rho_{\mathrm{loc\,max}}$.

We need now find the value of $\rho(z_0)^+$. We use the conservation of the stress, that boils down to the conservation of g, namely $g(\rho(z_0)^-) = g(\rho(z_0)^+)$. This yields $\rho(z_0)^+ = \rho_c$ or $\rho(z_0)^+$ is the other root of $g(\rho(z_0)^+) = g(\rho_c)$ with $\rho_c < \rho(z_0)^+ < \rho_{\mathrm{loc\,max}}$.

Suppose $\rho(z_0)^+$ is such that $\rho_c < \rho(z_0)^+ < \rho_{\mathrm{loc\,max}}$.

Near $\rho(z_0)^+$, we have

$$\partial_z v\big|_{z=z_0,+} = -k_d\left(1-\rho_\infty/\rho(z_0)^+\right) < 0.$$

Hence v is negative near $\rho(z_0)^+$, for instance on the interval $(z_0, z_0+\delta z]$. We recall here a simple reformulation of eq. (8):

$$2\eta\frac{\mathrm{d}\rho}{\mathrm{d}z}v = \rho(g(\rho)-g(\rho_c)).$$

On the interval $(z_0, z_0+\delta z]$, v is negative. Suppose we have $\frac{\mathrm{d}\rho}{\mathrm{d}z} \geq 0$ on this interval. We thus get $g(\rho) < g(\rho_c)$, which implies necessarily, that $\rho \geq \rho(z_0)^+$ and is thus in contradiction with $\frac{\mathrm{d}\rho}{\mathrm{d}z} \geq 0$.

A similar contradiction can be found if we suppose that $\frac{\mathrm{d}\rho}{\mathrm{d}z}$ is negative on this small interval.

We are left with the other scenario: $\rho(z_0)^+ = \rho_c$.

In that case, we again have a strictly decreasing velocity, and again a contradiction except if $\rho_c = \rho_\infty$. In that specific case, a plateau density profile of any length is possible.

As a conclusion, if there is a jump in the density profile, it is possible only from the single density value $\rho(z_0)^-$ that verifies $g(\rho(z_0)^-) = g(\rho_\infty)$ and $\rho(z_0)^- > \rho_{\mathrm{loc\,max}}$. We denote by ρ_f this value of density. ρ_f verifies $g(\rho_\infty) = g(\rho_f)$ and $\rho_f > \rho_{\mathrm{loc\,max}}$. The f stands for *free* because this specific profile characterizes the *cortical* regime where the layers are distinctly separated from one another. In this regime, the density goes from ρ_0 at the membrane to ρ_f, and then jumps to ρ_∞ and stays at that value until the boundary of the other layer is reached (where the density jumps back to ρ_f and continuously rises to ρ_0, as plotted in fig. 6).

Appendix D. Numerical methods

The simulations were performed using a finite-volume method to capture the sharp variations in the density profile. The mesh is constituted in 1D of 100 boxes with different sizes adapted to capture the critical behaviors at the midplane. The mesh was similarly adapted in 2D for a 60 by 60 pavement of boxes. The initial condition on the density profile is then propagated iteratively thanks to the integrated version of eqs. (7).

The first step is to update the velocity profile via the equilibrium of constraints equation. The second step is to propagate the concentration profile in time via the conservation of mass equation. This is done using a standard upstream/downstream explicit propagation, with autoadaptive time step.

For the simulations of sect. 3, implying temporal change of the domain size (slow movement of the distance between membranes), we renormalized the set of eqs. (7) in space. This results in a new advection term in the mass conservation equation, implying the time derivative of the domain size. The relative speed of the membrane planes was diminished until finding a convincing approximation of the steady state profiles.

For the simulations of sect. 4, the characteristics of the hole were monitored over time, for a sufficient amount of time, but not until complete relaxation of the system, to determine the outcome of the simulation. For instance, if the hole filled up till 90% of its initial depth, we concluded that the outcome of the experiment was a healed *lamellipodium*.

References

1. V.C. Abraham, V. Krishnamurthi, D.L. Taylor, F. Lanni, Biophys. J. **77**, 1721 (1999).
2. T.D. Pollard, G.G. Borisy, Cell **112**, 453 (2003).
3. J. Wu, I.A. Kent, N. Shekhar, T.J. Chancellor, A. Mendonca, R.B. Dickinson, T.P. Lele, Biophys. J. **106**, 7 (2014).
4. V. Achard, J.-L. Martiel, A. Michelot, C. Guérin, A.-C. Reymann, L. Blanchoin, R. Boujemaa-Paterski, Curr. Biol. **20**, 423 (2010).
5. J.-F. Joanny, K. Kruse, J. Prost, S. Ramaswamy, Eur. Phys. J. E **36**, 52 (2013).
6. H. Turlier, B. Audoly, J. Prost, J.-F. Joanny, Biophys. J. **106**, 114 (2014).
7. T.D. Pollard, L. Blanchoin, R.D. Mullins, Annu. Rev. Biophys. Biomol. Struct. **29**, 545 (2000).
8. O. Medalia, I. Weber, A.S. Frangakis, D. Nicastro, G. Gerisch, W. Baumeister, Science **298**, 1209 (2002).
9. G. Salbreux, G. Charras, E. Paluch, Trends Cell Biol. **22**, 10 (2012).
10. P.M. Bendix, G.H. Koenderink, D. Cuvelier, Z. Dogic, B.N. Koeleman, W.M. Brieher, C.M. Field, L. Mahadevan, D.A. Weitz, Biophys. J. **94**, 3126 (2008).
11. K. Kruse, J.-F. Joanny, F. Jülicher, J. Prost, K. Sekimoto, Eur. Phys. J. E **16**, 5 (2005).
12. J.-F. Joanny, F. Jülicher, K. Kruse, J. Prost, New J. Phys. **9**, 422 (2007).
13. A.C. Callan-Jones, F. Jülicher, New J. Phys. **13**, 093027 (2011).
14. R. Voituriez, J.F. Joanny, J. Prost, Europhys. Lett. **70**, 404 (2005).
15. S. Fürthauer, M. Neef, S.W. Grill, K. Kruse, F. Jülicher, New J. Phys. **14**, 023001 (2012).
16. S. Günther, K. Kruse, New J. Phys. **9**, 417 (2007).
17. G. Salbreux, J. Prost, J.F. Joanny, Phys. Rev. Lett. **103**, 058102 (2009).
18. K. Kruse, J.-F. Joanny, F. Jülicher, J. Prost, Phys. Biol. **3**, 130 (2006).
19. D.A. Lauffenburger, A.F. Horwitz, Cell **84**, 359 (1996).
20. I. Nedeva, G. Koripelly, D. Caballero, L. Chièze, B. Guichard, B. Romain, E. Pencreach, J.-M. Lehn, M.-F. Carlier, D. Riveline, Nat. Commun. **4**, 2165 (2013).
21. S. Diez, G. Gerisch, K. Anderson, A. Müller-Taubenberger, T. Bretschneider, Proc. Natl. Acad. Sci. U.S.A. **102**, 7601 (2005).
22. N. Watanabe, T.J. Mitchison, Science **295**, 1083 (2002).
23. F. Gerbal, P. Chaikin, Y. Rabin, J. Prost, Biophys. J. **79**, 2259 (2000).
24. V. Noireaux, R.M. Golsteyn, E. Friederich, J. Prost, C. Antony, D. Louvard, C. Sykes, Biophys. J. **78**, 1643 (2000).
25. F. Jülicher, K. Kruse, J. Prost, J.-F. Joanny, Phys. Rep. **449**, 3 (2007).
26. T. Kim, M.L. Gardel, E. Munro, Biophys. J. **106**, 526 (2014).